

— NODE REPORTS —

UWA Node

Single and double ion doping of metal oxide ZnO nano particles

The characterization of ZnO nano particles containing native defects and dopants continued the initiative of using multiple spectroscopic methods, here Positron Annihilation Lifetime (PALS), Coincidence Doppler Broadening (CDB), X-Ray Diffraction (XRD), and UV Spectra Analysis for Single and Double multicharged-Ion Doping (SDIDS). Each of these methods contributed to a significant expansion of our materials studies during the past year. They indicate the considerable increase in knowledge and capabilities with our ARC support. Underpinning the measurements was the improved synthesis of ZnO nano particles using a mild hydrothermal process with lower temperature and pressure for the advantages of free growth catalyst, low cost, and safest green technology. That method of

sample preparation enabled significant successes in tuning the band gap and obtaining consistent characterization of all materials, particularly of relevance now to the production of ZnO-based topological insulators. Our aim was to define the methods and to control the performance of this metal oxide for subsequent applications.

The Positron Annihilation Lifetime (PALS)

measurements gave two-fitted lifetimes and an average positron lifetime [$\tau_{av} = (I_1\tau_1 + I_2\tau_2)/(I_1 + I_2)$] as shown in the table. The longest lifetimes occurred for Ru^{3+} ions among the single-doped and for $\text{Sn}^{4+} + \text{Co}^{2+}$ for the double-doped ZnO samples. These lifetimes reflect the average electron density at the site of annihilation. Other techniques were used for indications of the chemical environment or how the band gap is influenced by the defect energy levels overlapping in the band region.

Table 1: Positron lifetimes of undoped, single- and double- doped ZnO. Note that τ = lifetime and I = intensity.

Sample	$\tau_1 \pm 3.3$ (ps)	$I_1 \pm 3\%$	$\tau_2 \pm 8.5$ (ps)	$I_2 \pm 3\%$	τ_{av} (ps)
Undoped ZnO	228.9	68.2	413.0	31.8	287.5
ZnO(Ag^+)	226.3	61.2	390.4	38.8	290.0
ZnO(Pd^{2+})	247.5	75.8	445.6	24.2	295.5
ZnO(Ru^{3+})	243.3	69.8	416.2	30.2	295.6
ZnO($\text{Ag}^+ + \text{W}^{6+}$)	230.4	69.3	419.6	30.7	288.4
ZnO($\text{Ag}^+ + \text{Pd}^{2+}$)	223.3	63.7	402.1	36.3	288.2
ZnO($\text{Sn}^{4+} + \text{Co}^{2+}$)	237.3	70.3	426.6	29.7	293.4

XRD scans of Ag^+ single-doped ZnO, shown in Figure 24, indicated evidence of a residual phase of silver ions but a low concentration of the dopants (of 1%M) limited the extensive attempts for quantitative measurements. Characteristic peaks of impurity phases were absent for Ru^{3+} and Pd^{2+} -doped ZnO. All the strong diffraction peaks were at 2θ values of 31.72° , 34.35° , 36.29° , 47.51° , 56.62° , and 62.83° , and correspond to the following lattice planes (hkl): (100), (002), (101), (102), (110) and (103), respectively, which indicated that only single-phase wurtzite ZnO was present in the samples. This characterization was essential when the method of preparation was changed and/or doping varied and before lifetime spectroscopy was made.

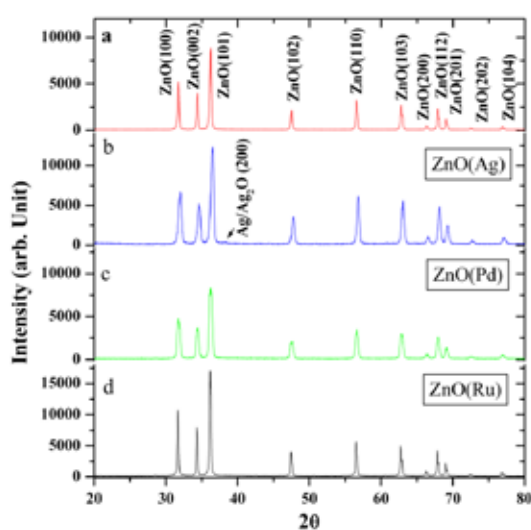


Figure 24: XRD spectra for (a) pure ZnO; (b) Ag^+ doped ZnO; (c) Pd^{2+} doped ZnO; (d) Ru^{3+} doped ZnO.

Band gap energy of doped ZnO nanoparticles

The effect of doping on the band gap of ZnO nanoparticles was studied using UV-Vis-NIR spectroscopy in the wavelength range of 300–800 nm. In Figure 25, typical UV-Vis scans indicate a red shift of absorbance wavelength in doped ZnO nanoparticles. The band gap of undoped ZnO was measured also using the four-probe method to be 3.25 eV, which is within normal variations of 3.37 eV since it depends on the synthesis route and the presence of various defects. Doping of Ru^{3+} , Pd^{2+} and Ag^+ into ZnO reduced the band gap and was shown to enhance the photo response of ZnO extending even to the visible range. In contrast, couple-dopants decreased the band gap significantly. The tuning of the band gap has been improved considerably in couple-doping of ZnO. The Ru^{3+} decreased the band gap energy from 3.25 to 3.13 eV, i.e. a nearly 4% decrease. However, among the couple-doped samples, $\text{Sn}^{4+}+\text{Co}^{2+}$ decreased the band gap further to 2.84 eV i.e. by 12.6% which is very significant for nanoparticles synthesized from the present simple method of a mild hydrothermal process.

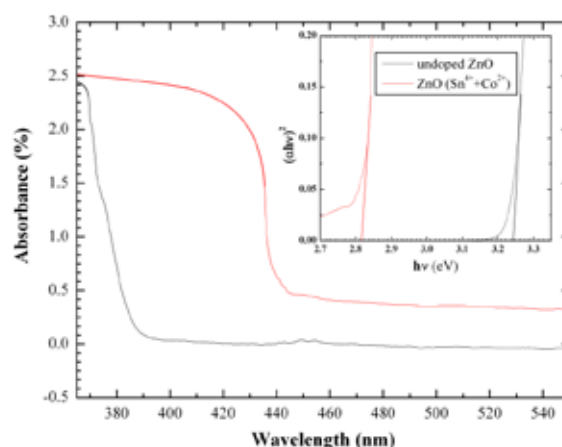


Figure 25: UV spectra of single-doped Ag^+ and undoped ZnO.

It was found that doping of Sn^{4+} results in new trapping states, which can introduce new electronic energy states into the band of ZnO, to form a new lowest unoccupied molecular orbital i.e. valence band (interband trapped states). Similarly, doping Co^{2+} with ZnO results in a reduced gap due to the coupling effect of the 3d orbitals of Co^{2+} and Zn^{2+} ions which constitute the conduction band of doped ZnO. For Ni doped ZnO, the 3d electrons of Ni hybridize strongly with the 2p electrons of O resulting in a widening of the valence band thereby increasing its maximum value. We found that Co^{2+} doping also led to the introduction of a shallow occupied Co 3d state. Also Sn^{4+} being smaller in size compared to V_{Zn} and more reactive than Co^{2+} , it may replace the Zn^{2+} vacancy site (V_{Zn}). Thus $\text{Sn}^{4+} + \text{Co}^{2+}$ couple-doping, with this combined effect of both dopants going substitutional, led to a maximum shift in the absorbance wavelength compared with all other samples. The $\text{Ag}^+ + \text{W}^{6+}$ and $\text{Ag}^+ + \text{Pd}^{2+}$ couple-doped samples also show a good reduction

in the bandgap compared to single-doped ZnO. The method proved reliable.

The CDB measurements were made for further elemental characterization using a BaF_2 detector and a high purity HpGe detector, with 1.1 keV full-width-at-half-maximum of the 662 keV γ -line of ^{137}Cs radioactive source and a constant channel width of 0.192 keV/channel. The CDB momentum ratio curves indicated that single Ru^{3+} -doping had a significant effect, particularly referenced against pure ZnO. The single Ag^+ and Pd^{2+} dopants occupy interstitial sites of the ZnO lattice while Ru^{3+} can replace the Zn vacancy substitutionally. Also the $(\text{Ag}^+ + \text{Pd}^{2+})$, $(\text{Ag}^+ + \text{W}^{6+})$ and $(\text{Sn}^{4+} + \text{Co}^{2+})$ double-dopings of the ZnO lattice showed CDB ratio curves similar to Ru^{3+} single-doped ZnO. The double-doping showed significant decreases in the band gap energy compared to single doping and a maximum decrease in band gap of about 12.6%.

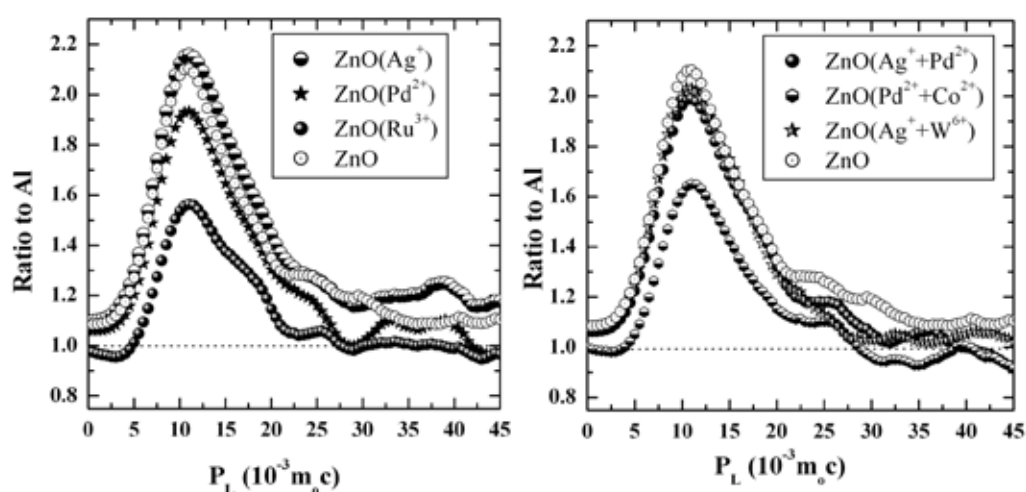


Figure 26: CDB ratio spectra for singly doped and couple doped ZnO with Al as the reference.

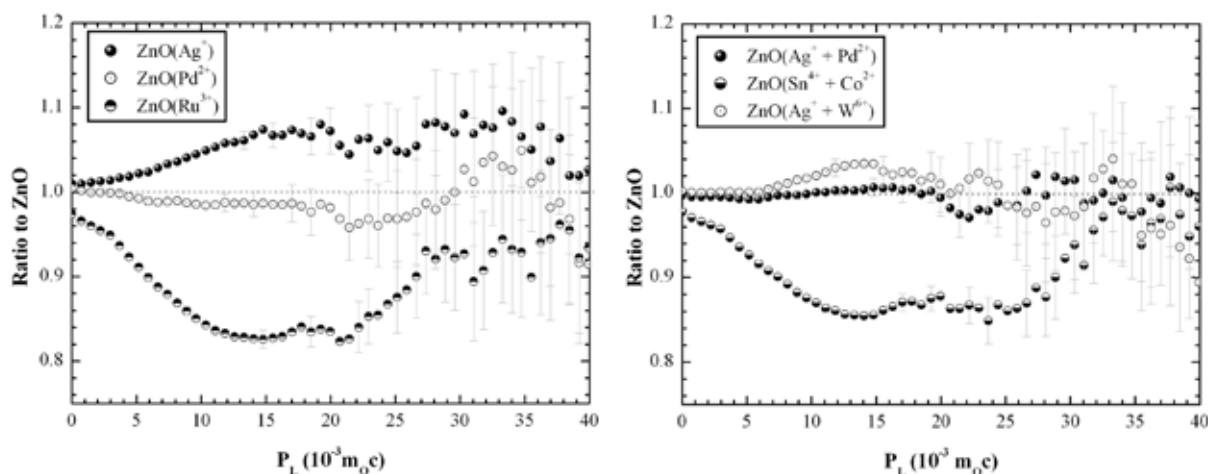


Figure 27: CDB ratios of singly (left) and couple (right) doped ZnO with undoped ZnO as a reference.

The momentum ratio curves, with undoped ZnO as the reference, clearly indicate dopants in interstitial or substitutional sites. Ru³⁺ single-doping has a profound effect on the ratio curves particularly with ZnO as a reference. It can be inferred that Ag⁺ and Pd²⁺ occupy interstitial sites of the ZnO lattice, while Ru³⁺ will replace Zn²⁺ substitutionally. The dopant in the interstitials seems to be more effective in reducing the nanoparticle size, as shown by XRD results. The Ag⁺ and Pd²⁺ doped ZnO are of 29.20 nm and 28.76 nm (respectively), compared to the size of undoped ZnO. The ionic size and charge state of the dopants decide which dopant goes where. The Sn⁴⁺, Co²⁺ and W⁶⁺ as codopants go into ZnO lattice substitutionally while others go interstitially. Therefore, the CDB ratio curves can serve as an indicator of whether the dopants are substitutional or interstitial. The Sn⁴⁺+Co²⁺ double-doped ZnO is interesting as it decreases the band gap by 12.6%, a better result compared to single metal ion doping. It is expected that reduction of the band gap will push the photo response of ZnO to the visible range. The presence of transition metal ions trapped electrons

interstitially which resisted the recombination of electrons with holes. Such materials are promising for photo-catalysis applications and for studies of topological phases. The main benefit was, however, verifying and quantifying the doping procedure.

Influence of polar groups in binary polymer blends on positronium formation

This work studied the role of the polar group with unconjugated oxygen on the inhibition of positronium (Ps) formation in two binary blends, made from a set of chosen constituent polymers with polar and weakly polar groups (non-polar). The two polymer blends were selected with different conjugation groups, in general with lower overall energy and different stability, to form a conjugated system with overlapping (delocalized) p-orbitals across adjacent aligned p-orbitals which may bridge adjacent single bonds. We chose PVC-EVA (Poly Vinyl Chloride-Ethylene Vinyl Acetate) in which EVA contains a strong polar group of the type -C=O (unconjugated) and PVC-SAN (Poly Vinyl Chloride-Styrene Acrylonitrile) in which SAN is nearly non-polar or very weakly polar

in character due to the presence of the $\text{C}\equiv\text{N}$ group. According to the polar group concept the atoms with a difference in electro-negativity less than 1.7 results in a covalent bond of a polar nature and when the difference is less than 0.5 a non-polar covalent bond is formed. The carbonyl group ($-\text{C}=\text{O}$) in the acetate part of EVA shows a difference in the electro-negativity between C (2.55) and O (3.44) of 0.89 indicating a strong polar group. For the SAN polymer, the cyanidyl ($-\text{C}\equiv\text{N}$) group is non-polar or very weakly polar as the difference in the electro-negativity between C (2.55) and N (3.04) is 0.49. In both blends of this study, the PVC contains chlorine which is a strong inhibitor of Ps formation like other halogens. Possible interaction paths are indicated in Figure 28, with (a) PVC-EVA and (b) PVC-SAN polymer blends.

The contributions from different electron and positron states are evident in Figure 29. Three regions are identified; the low momentum region

from 0 to 3 momentum units corresponds to p-Ps annihilation and is generally observed as the narrow component of the CDB spectra. The intermediate momentum region from 3 to 13 momentum units corresponds to annihilation of σ - and π -bond valence electrons of the polymer blend and the high-momentum region above 15 momentum units corresponds to annihilation of core electrons with the positron of o-Ps. The ratio curves exhibit non-Gaussian distributions for different compositions with different peak heights and widths. In contrast, the ratio curves in pure metals, with simple electronic structure, are readily approximated by Gaussian distributions. The peak heights infer that the probability of particular types of electrons participating in the annihilation process is high or low. Widening of the peak width can be attributed to contributions from p-Ps and o-Ps to annihilation.

The contribution of the strong polar acetate group in EVA to positron annihilation with the electrons of unconjugated oxygen ($-\text{C}=\text{O}-$) was revealed (see Figure 29), by the ratio curves for the Coincidence Doppler Broadening (CDB) spectra of PVC-EVA blends and of the pure EVA with respect to pure PVC. The inset CDB spectra of the PVC-EVA blends shows each spectrum normalized to the same total counts and indicates the accuracy obtained in the measurements to enable the ratio determinations. The peak around $17 P_L$ ($10^{-3} m_0 c$) in the momentum distribution curves is attributed to the unconjugated oxygen ($-\text{C}=\text{O}-$) group.

The ortho-Ps intensity indicated the unconjugated oxygen shows about a 28% Ps reduction even in the presence of a strong Ps inhibiting halogen (Cl^-). In contrast, this effect was not seen in the PVC-SAN blends (see Figure 30) since SAN contains a weakly

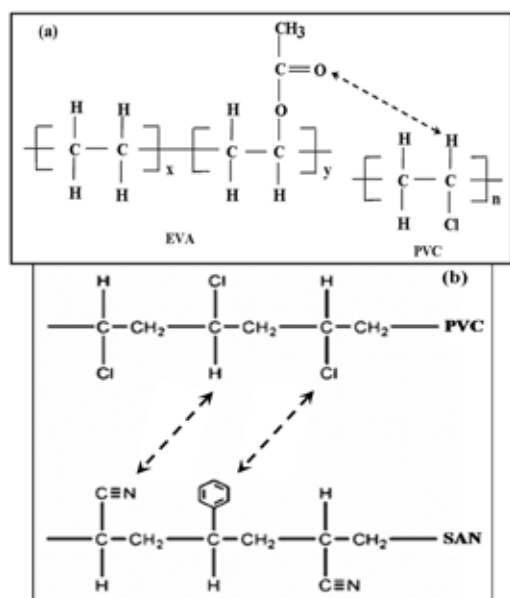


Figure 28: Illustration of possible interaction paths in (a) PVC-EVA and (b) PVC-SAN polymer blends.

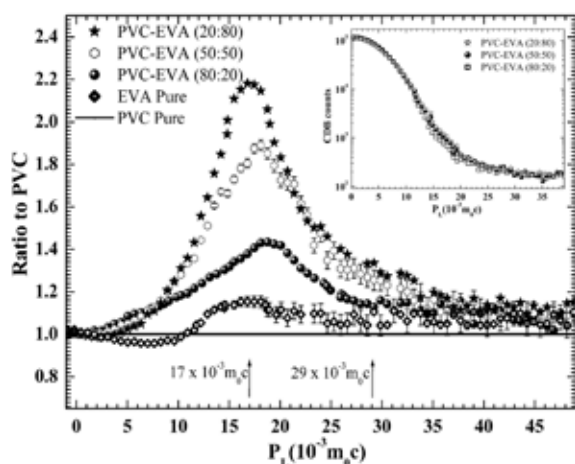


Figure 29: Ratio curves for the CDB spectra of PVC-EVA blends and pure EVA with respect to pure PVC. In the inset are CDB spectra of the PVC-EVA blends with each spectrum normalized to the same total counts.

polar (nonpolar) acrylonitrile group ($C\equiv N$). Our results indicate the chlorine of PVC in the blends is a major contributor to Ps inhibition through the formation of a (Cl^-e^+) bound state, but the unconjugated oxygen in EVA of the PVC-EVA blend also plays a similar, but lesser, role.

These studies have identified the relationships between the oxygen-containing groups and positronium formation, as well as the elemental variations around defect sites. The work is continuing with double and ternary polymer blends used in industrial and scientific fields, which require multifunctional and high performance materials without the limitations of single polymeric materials.

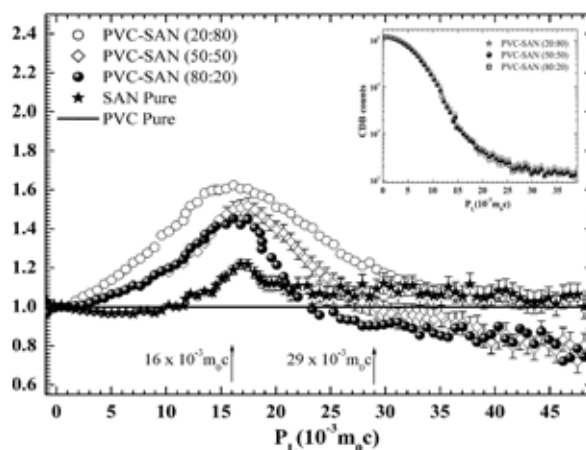


Figure 30: Ratio curves for the CDB spectra of PVC-SAN blends and pure SAN with respect to pure PVC. In the inset are CDB spectra of the PVC-SAN blends with each spectrum normalized to the same total counts.

Positron annihilation in off-stoichiometric and Ta-doped Zn_2TiO_4

Recent interest in Zn_2TiO_4 , as an electronic ceramic that displays ionic conduction, has focused on the charge compensation mechanisms exhibited when the material contains excess Ti or is doped with pentavalent Ta ions. The stoichiometric material Zn_2TiO_4 has an inverse spinel structure with a tetrahedral Zn ion and octahedral Zn and Ti ions. It is known that compositions of $Zn_2TiO_4 + xTiO_2$, when equilibrated in air at temperatures above $945^\circ C$, form a single-phase Zn_2TiO_4 structure for x up to ~ 0.33 and attributed the charge compensation mechanism to tetrahedral Zn vacancies. Also, studies of $Zn_{(2-x)/2}Ti_{(1-x)}Ta_xO_4$ compositions in which cation vacancies were deposited as the charge compensators using neutron diffraction provided evidence of octahedral vacancies for $x > 0.1$.

XRD and SEM measurements then showed that all $\text{Zn}_2\text{Ti}_{1-5x/4}\text{Ta}_x\text{O}_4$ ($0 < x < 0.4$) samples were essentially single-phase Zn_2TiO_4 . However, Ta doping increased the lattice parameter slightly and, when x exceeded 0.24, additional weak reflections and a broadening of the main spinel-

type reflections indicated the gradual development of the tetragonal phase. Also samples doped with 0.4 formula units (f.u.) of Ta showed a very small amount of second-phase material. SEM micrographs of nominally stoichiometric Zn_2TiO_4 and with 0.4 f.u. of Ta are shown in Figure 31.

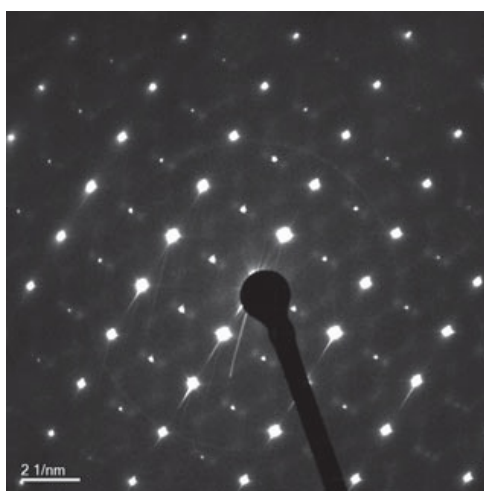
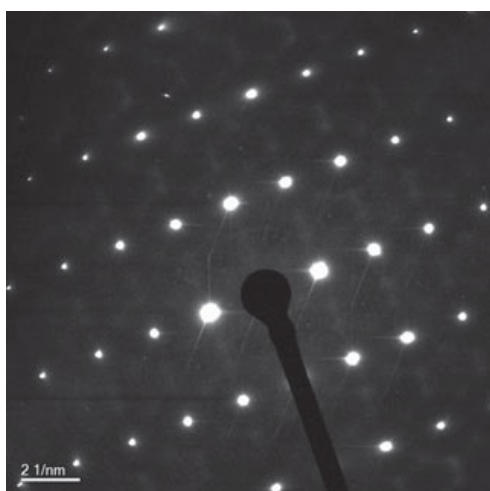


Figure 31: Selected-area diffraction patterns of Zn_2TiO_4 samples with brightness and contrast adjusted from the original files. LEFT, nominally stoichiometric cubic sample, taken down the $[112]_c$ zone axis, showing weak diffuse scattering as pairs of nodes at $G_{\text{SP}} \pm (1-10)$ and symmetry-related positions plus additional arcs of very weak diffuse scattering around strong Bragg reflections. RIGHT, tetragonal sample, taken down the $[011]_t$ zone axis and showing similar diffuse scattering to the cubic sample. Note that the tetragonal sample has additional weak Bragg reflections at $(100)_t$ sitting between the pair of diffuse nodes.

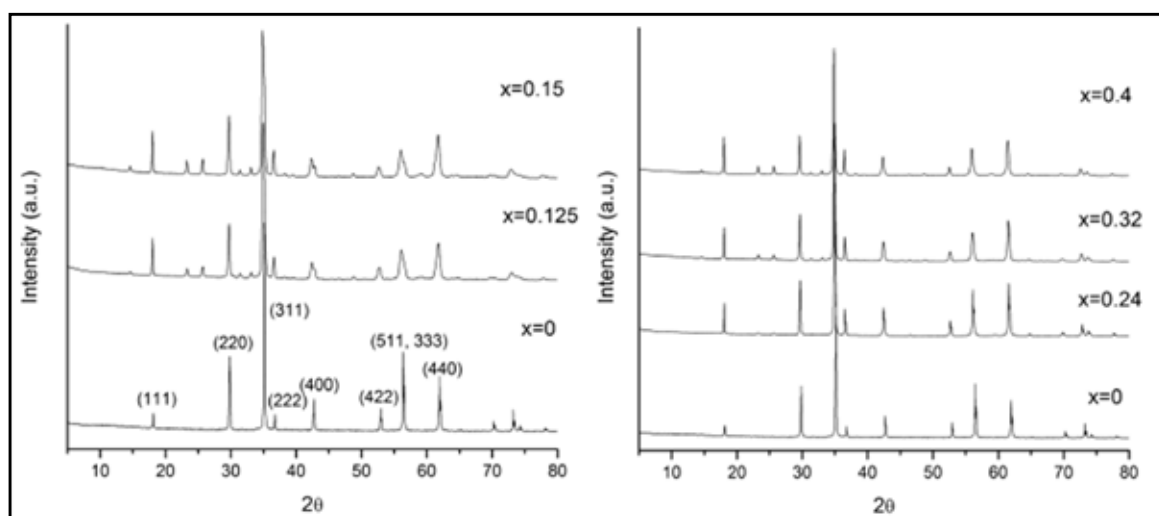


Figure 32: Right: XRD patterns for the $\text{Zn}_2\text{Ti}_{1-5x/4}\text{Ta}_x\text{O}_4$ samples; left: XRD patterns for the $\text{Zn}_{2-x}\text{Ti}_{1-2x}\text{Ta}_x\text{O}_4$ samples.

Single-phase Ta-doped Zn_2TiO_4 samples showed a gradual increase in the positron lifetime after the Ta concentration was increased to 0.2 f.u. This behavior differs from that observed in other systems, where cation vacancies have been evidenced as the applicable charge compensators. This suggests that cation vacancies are not the appropriate charge compensators in the Zn_2TiO_4 systems which were investigated. Other compensation mechanisms such as the creation of interstitial oxygen ions are presumed to be operative. No evidence of cation vacancy formation was found in the Ti-rich samples, contrary to suggestions in the literature.

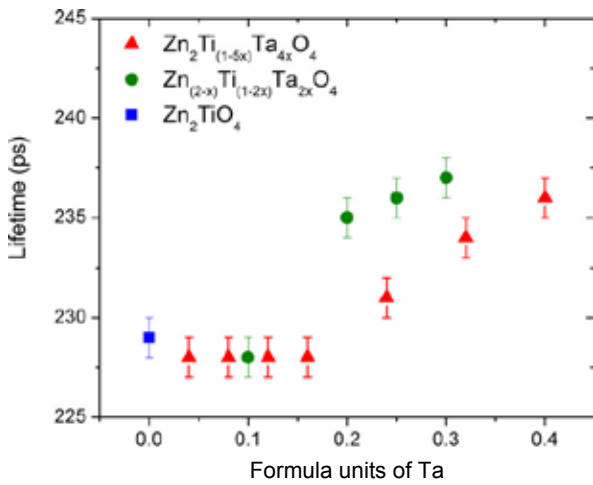


Figure 33: Positron lifetimes as a function of units of Ta.

The small lifetime increase is most likely associated with the increased lattice parameter arising from the development of the tetragonal phase. The variation in the lattice parameter for the cubic samples $\text{Zn}_{2-x}\text{Ti}_{1-2x}\text{Ta}_{2x}\text{O}_4$ and $\text{Zn}_2\text{Ti}_{1-5x/4}\text{Ta}_{x/4}\text{O}_4$ are significant; the first sample had a lattice parameter of 0.8495 nm and the latter of 0.848 nm for $x \sim 0.1$. Alternatively, cation vacancies in Zn_2TiO_4 ceramics could trap holes to a sufficient degree to prevent the Coulomb attraction of the positrons and hence positron trapping to produce longer lifetimes might be negated. While theoretical investigations are necessary to resolve these issues, the techniques and outcomes were significant because they indicated the methods and the variations required for control of the interesting lattice parameters, which has similarities with oxides being tested for topological phase characteristics.

While Zn vacancies are regarded as the charge compensators in Ti-rich Zn_2TiO_4 , no evidence of cation vacancies was deduced from positron annihilation lifetime spectroscopy (PALS) of essentially single-phase samples containing up to 13 wt% excess TiO_2 . Similarly there was no strong evidence of cation vacancies in Ta-doped samples, targeted to contain either tetrahedral or octahedral vacancies, although there was a small increase in lifetime as the doping level increased and the structure changed from cubic to tetragonal.